Hepatic Radiofrequency Ablation

Monitoring of Ablation-Induced Macrophage Recruitment in the Periablational Rim Using SPION-Enhanced Macrophage-Specific Magnetic Resonance Imaging

Federico Collettini, MD,*† Julia Brangsch, VMD,*‡ Carolin Reimann, VMD,*‡ Julius Chapiro, MD,§ Lynn Jeanette Savic, MD,* Rebecca Buchholz, MSc,‖ Sarah Keller, MD,* Bernd Hamm, MD, PhD,* S. Nahum Goldberg, MD,¶ and Marcus R. Makowski, MD, PhD*#**††

Objectives: Macrophages accumulating in the periablational rim play a pivotal role in initiating and sustaining the perifocal inflammatory reaction, which has been shown to be at least 1 of the mechanisms responsible for the systemic pro-oncogenic effects of focal hepatic radiofrequency ablation (RFA). Herein, we tested the hypothesis to use superparamagnetic iron oxide nanoparticle (SPION)–enhanced magnetic resonance imaging (MRI) for noninvasive quantification of iron-loaded macrophages in the periablational rim of VX2 tumor-bearing rabbits.

Materials and Methods: Twelve VX2 tumor-bearing rabbits underwent MRI immediately after and up to 3 weeks after focal hepatic RFA. For noninvasive quantification of macrophage accumulation in the periablational rim, animals were scanned before and 24 hours after SPION injection. T2*-weighted images were analyzed and correlated with histopathological and immunohistochemical findings. Furthermore, correlations with quantitative measurements (ICP-MS [inductively coupled plasma–mass spectrometry] and LA-ICP-MS [laser ablation–ICP-MS]) were performed.

Results: SPION-enhanced T2*-weighted MRI scans displayed a progressive increase in the areas of signal intensity (SI) loss within the periablational rim peaking 3 weeks after RFA. Accordingly, quantitative analysis of SI changes demonstrated a significant decline in the relative SI ratio reflecting a growing accumulation of iron-loaded macrophages in the rim. Histological analyses confirmed a progressive accumulation of iron-loaded macrophages in the periablational rim.

The ICP-MS and LA-ICP-MS confirmed a progressive increase of iron concentration in the periablational rim.

Conclusions: SPION-enhanced MRI enables noninvasive monitoring and quantification of ablation-induced macrophage recruitment in the periablational rim. Given the close interplay between ablation-induced perifocal inflammation and potential unwanted tumorigenic effects of RFA, SPION-enhanced MRI may serve as a valuable tool to guide and modulate adjuvant therapies after hepatic RFA.

Key Words: molecular imaging, magnetic resonance imaging, radiofrequency ablation, liver cancer, inflammation

For the past 3 decades, hepatic radiofrequency ablation (RFA) has been extensively tested and currently represents a well-recognized and broadly used minimally invasive therapy for patients with primary and metastatic liver cancer.[1,2] Despite widespread clinical use, there is ever increasing awareness that focal tumor ablation may walk along with long-term unknown, unintended systemic effects. In recent years, several groups have advocated that heat-based ablative techniques may stimulate local and distant tumor growth by means of proinflammatory, proangiogenic, and proregenerative pathways.[3,4] In several studies, these "off-target" tumorigenic effects have been linked to the reactive inflammatory response to RFA taking place in the portion of liver parenchyma surrounding the zone of ablation (periablational rim) and subjected to sublethal thermal damage.[3–5] Liver injury initiates a complex sequence of reactive cellular responses, starting from inflammation and proceeding to tissue repair.[6] Both resident (Kupffer cells [KCs]) and monocyte-derived macrophages (MoMFs) hold a critical position in all phases of hepatic response to injury.[7] Thanks to their high plasticity, macrophages switch between different phenotypes (inflammatory and anti-inflammatory) and exert various in part opposing functions according to the phase of injury and in response to signals from the hepatic microenvironment.[7–9]

After hepatic RFA, macrophages accumulate in the periablational rim and orchestrate the internal wound healing process through the release of inflammatory cytokines (eg, interleukin 6 [IL-6]) and growth factors (eg, hepatocyte growth factor [HGF]/c-Met, vascular endothelial growth factor [VEGF]).[4,10] These key mediators have been shown to be locally and systemically upregulated after RFA, and several studies have shown that unwanted tumorigenic effects of hepatic RFA can be blocked by their pharmacologic targeting.[5,11–13]

Because macrophage recruitment into the periablational rim plays a key role in RFA-induced cytokine and growth factor production, noninvasive quantification of macrophages in the periablational rim would be a valuable instrument to monitor and ultimately modulate RFA-induced tissue reactions.

Tissue inflammation and in particular macrophage accumulation can be imaged in vivo using superparamagnetic iron oxide nanoparticle (SPION)–enhanced magnetic resonance imaging (MRI).[14–16] The SPIONs are phagocytosed by macrophages after intravenous injection,

and because of their ability to shorten T1, T2, and T2*, they induce measurable loss of MRI signal intensity (SI).[17] Experimental studies with SPION-enhanced MRI for the assessment of macrophage accumulation have been successfully performed in various diseases models including inflammation and cancer.[18–20] In the context of hepatic RFA, SPION-enhanced MRI has been successfully used for early visualization of ablative margins after ablation.[21–23] However, to the best of our knowledge, no studies have evaluated the use of SPION-enhanced MRI for the noninvasive monitoring and quantification of RFA-induced inflammatory reactions.

The purpose of this study was to prospectively evaluate the use of SPION-enhanced MRI for noninvasive quantification of RFA-induced macrophage accumulation in the periablational rim of VX2 tumor-bearing rabbits.

MATERIALS AND METHODS

VX2 Rabbit Liver Tumor Model

Experiments were approved by the local regulatory authority (State Office for Health and Social Affairs Berlin [LAGeSo]) and conducted in compliance with the regulations of the Federation of European Laboratory Animal Science Associations. All procedures were performed under general anesthesia using subcutaneous medetomidine hydrochloride (Cepetor, 0.25 mg/kg; CP-Pharma, Burgdorf, Germany), and ketamine hydrochloride (Ketamin, 30 mg/kg, CP-Pharma, Burgdorf, Germany). In addition, analgesic therapy was administered intravenously during surgery (buprenorphine [Temgesic], 0.03 mg/kg; Indivior Europe Limited, Dublin, Ireland) and subcutaneously for the following 3 days after (carprofen [Rimadyl], 4.0 mg/kg; Berlin, Germany]) all surgical procedures.

Twelve New Zealand white rabbits (n = 12; age, 11–17 weeks; weight, 3.0–3.5 kg; Charles River Laboratories, Sulzfeld, Germany) were treated. Four additional rabbits (n = 4) were used to generate the tumor chunks (donor animals). Rabbits were housed on a 12-hour light-dark cycle in a pathogen-free animal facility with food and water ad libitum.

After anesthesia, 1 mL (approximately 1 million cells) of a freshly prepared suspension of cells derived from an established VX2 tumor cell line was injected in the gluteal muscle of the hind thigh of the donor rabbits. After confirmation of tumor growth by ultrasound imaging, donor animals were killed, and the hind limb tumors were harvested. Macroscopically necrotic tissue was removed with a surgical blade, and the tumor tissue was ground into 1 mm³ chunks. To attain the growth of a solitary liver tumor, tumor chunks were implanted in the left liver lobe of the 12 experimental rabbits using an 18-gauge catheter during open laparotomy. The Glisson's capsule was closed using an absorbable thrombogenic material (Gelfoam; Pfizer Inc, New York, NY) to circumvent peritoneal spread. The wound was then sutured in double layers. Tumor-bearing animals with a confirmed hepatic tumor growth between 1 and 2 cm at the implantation site underwent RFA of the hepatic VX2 tumor. The experimental design of the study is summarized in Figure 1.

Radiofrequency Ablation

Radiofrequency ablation was performed during laparotomy using a commercially available RF generator (1500X RF; AngioDynamics, Latham, NY) equipped with a perfused 14-gauge RF needle applicator with a 1-cm exposed tip.[24] A self-adhesive neutral electrode was applied on the animal's shaven back. The needle applicator was advanced centrally into the tumor to obtain complete tumor ablation. Isotonic saline solution was continuously instilled into the coagulation zone via microbores in the needle tip at a flow rate of 40 mL/h. The power output was calibrated to ensure a mean tip temperature of 70°C for 5 minutes.
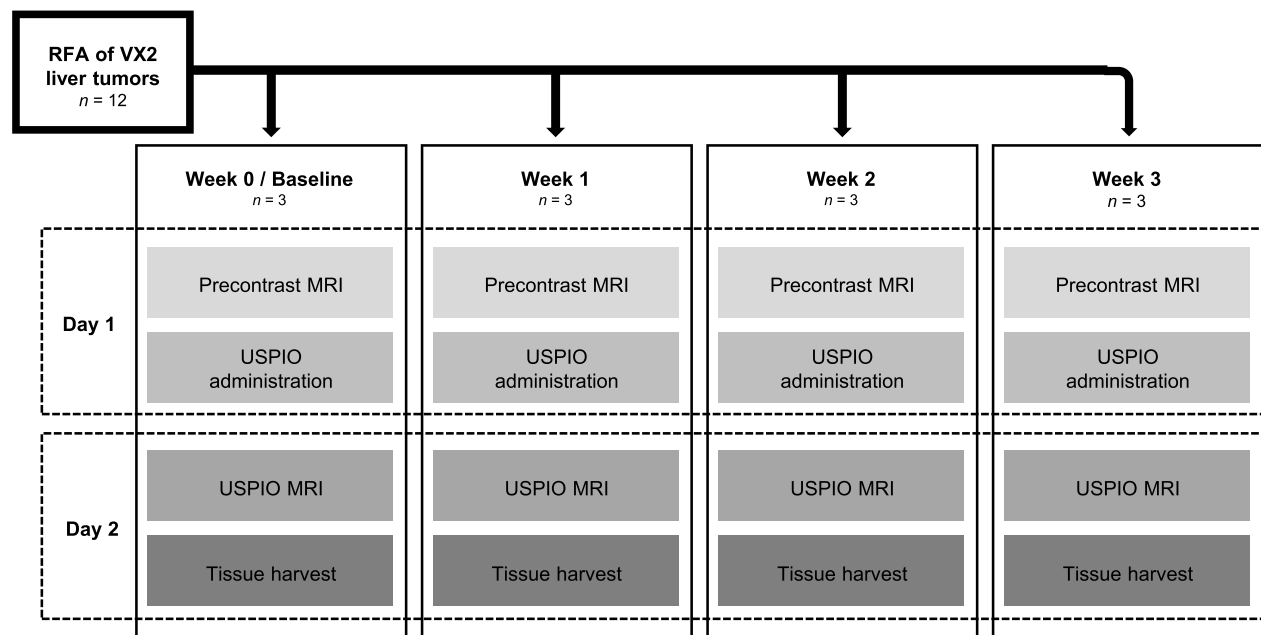
FIGURE 1. Experimental study design. The flow chart illustrates the magnetic resonance imaging (MRI) studies carried out on 4 experimental groups at consecutive time points. Imaging studies were completed (1) at baseline on week 0 (n = 3; 1–2 days), (2) 1 week (n = 3; 7–8 days), (3) 2 weeks (n = 3; 14–15 days), and (4) 3 weeks (n = 3; 21–22 days) after radiofrequency ablation (RFA). At each time point, imaging studies were conducted on 2 consecutive days. On the first day, a precontrast MRI was performed followed by the administration of superparamagnetic iron oxide nanoparticles (SPIONs) through an ear vein. Twenty-four hours after SPION administration, on day 2 of each time point, a second MRI scan (SPION MRI) was performed. Immediately after SPION MRI, animals were killed and the livers were harvested for histologic analysis.

In Vivo Magnetic Resonance Experiments

Magnetic resonance imaging was performed on a 1.5-T unit (Avanto; Siemens Healthcare Solutions, Erlangen, Germany) with a clinically approved 4-channel knee coil. The first MRI examination, performed on day 1 of each time point, served as a baseline study before injection of the SPION-based macrophage-specific agent (Fig. 1). After precontrast MRI scan, the SPION-based contrast agent ferucarbotran (Resovist; Bayer Pharma AG, Japan; particle size, 60 nm) was administered intravenously through an ear vein (0.023 mL/kg) in a single injection. The second MRI scan was performed 24 hours after SPION administrated ion. This interval allowed clearance of iron particles from the blood circulation and complete phagocytosis by macrophages outside the reticuloendothelial system.[25]

The MRI protocol included morphologic axial T2-weighted turbo spin echo sequences (repetition time/echo time, 4100/77 milliseconds; field of view, 160 mm; matrix, 512 × 358; spatial resolution, 0.3 × 0.4 mm; slice thickness, 3 mm; flip angle, 150 degrees) as well as unenhanced (day 1 of each time point) and SPION-enhanced (day 2 of each time point) T2*-weighted images using the following sequences: 2-dimensional fast low-angle shot (repetition time/echo time, 280/23 milliseconds; field of view, 220 mm; matrix, 384 × 300; spatial resolution, 0.6 × 0.7 mm; slice thickness, 2 mm; flip angle, 30 degrees) and multiple echo recombined gradient echo (repetition time/echo time, 590/17 milliseconds; field of view, 200 mm; matrix, 256 × 192; spatial resolution, 0.8 × 1.0 mm; slice thickness, 3 mm; flip angle, 30 degrees).

Magnetic Resonance Data Analysis

Magnetic resonance data analysis was performed by 2 board-certified radiologists (F.C. and M.R.M., both with 10 years of experience in advanced liver imaging) working in consensus. To quantify the accumulation of SPION-loaded macrophages in the periablational rim, the area of the periablational rim demonstrating signal loss on SPION-enhanced T2*-weighted images (dark pixel area) was segmented and measured at each time point using ImageJ software (Version 1.51)[26] (Figs. 2A, B). Furthermore, quantitative analyses of SI changes of the periablational rim after SPION administration were performed at each
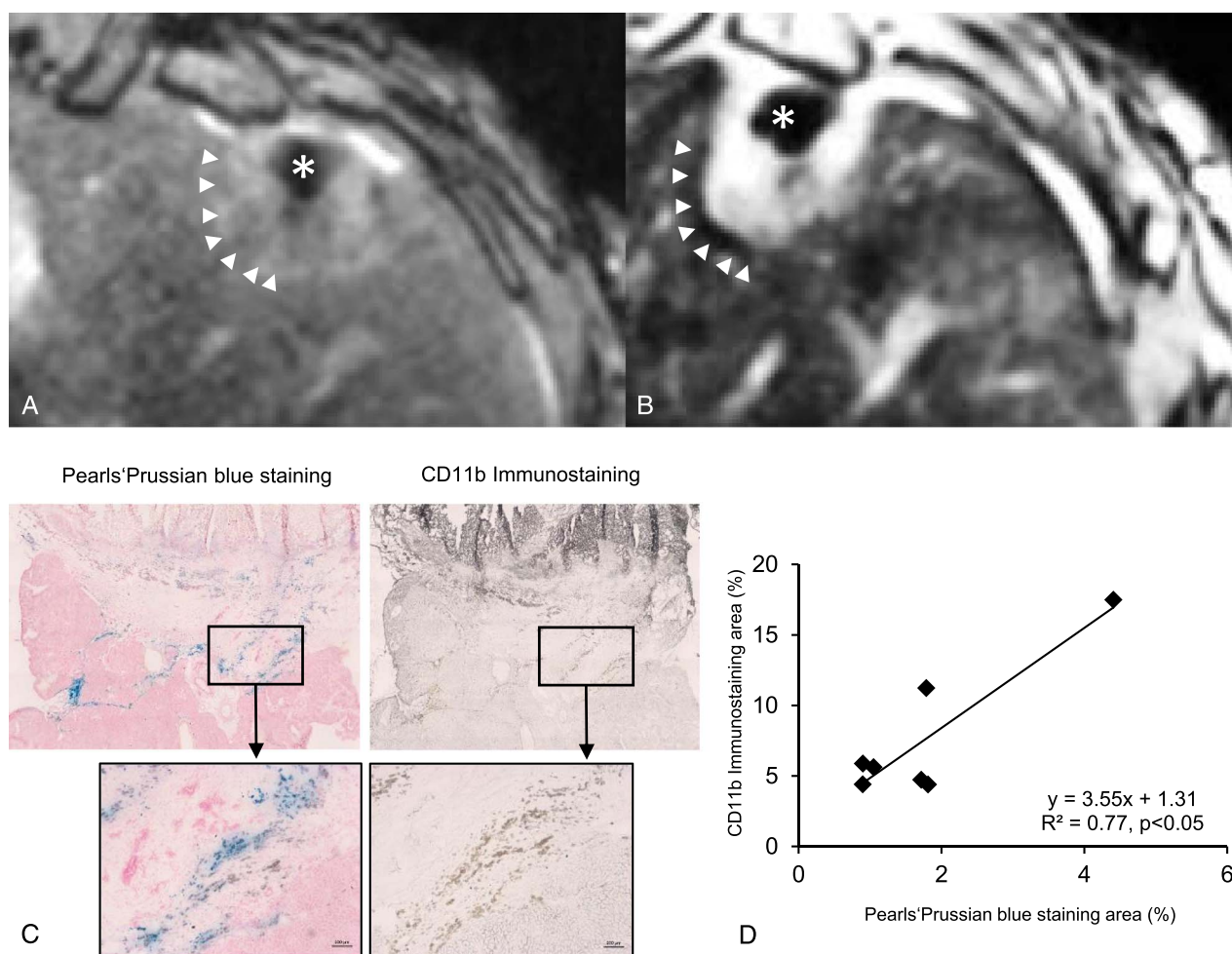
FIGURE 2. In vivo macrophage imaging using SPION-enhanced MRI and ex vivo histological analysis. Axial T2*-weighted images obtained 2 weeks after RFA of a VX2 tumor in the left liver lobe, (A) before and (B) 24 hours after intravascular administration of SPION. Precontrast T2*-weighted images show a slightly hyperintense ablation zone surrounding the markedly hypointense needle track (asterisk). No areas with signal loss can be seen in the periablational rim. On SPION-enhanced images, a band-like area of low signal (arrowheads) due to the presence of SPION-loaded macrophages can be seen in the periablational rim. C, Representative histological section of the periablational rim 4 weeks after ablation. A broad accumulation of iron oxide particles using Perls Prussian blue staining (left hand) was shown, which was clearly colocalized with macrophages using CD11b immunohistochemical staining (right hand). Scale bars on magnifications indicate 100 μm. D, A strong correlation was shown between CD11b immunostaining areas (%) and Perls Prussian blue staining areas (%) ($y = 3.55x + 1.31$, $R^2 = 0.77$, $P < 0.05$).

time point. Pre-SPION and post-SPION MRI scans were visually matched on a dedicated DICOM-based software (OsiriX Version 5.6; OsiriX Foundation, Geneva, Switzerland) on the same anatomical level using the zone of ablation as a marker. Three regions of interest (ROIs) with an area of 2 to 6 mm^3 were placed in the rim of liver tissue surrounding the visible ablation zone (periablational rim) as well as in normal liver tissue on the contralateral lobe. The mean value of the 3 ROIs was calculated. The relative SI (rSI) was determined by dividing the mean SI measured in the ROI placed in the periablational rim by that of the ROI placed in the normal liver tissue on the contralateral lobe. Signal changes over time were quantified by calculating the rSI ratio, which was defined as the quotient of the rSI in post-SPION and pre-SPION MRI.[27]

Histology and Immunohistochemistry

Immediately after SPION MRI, animals were killed using pentobarbital-natrium (400 mg/kg intravenous, NarcoreN; Boehringer Ingelheim Vetmedica GmbH). To determine macrophage accumulation in the periablational rim, the ablated left liver lobes were harvested at each of the 4 time points directly after SPION-enhanced MRI. For each time point, 3 animals were used. Tissue was fixed in 4% formaldehyde, embedded in paraffin, and sliced into 5-μm-thick slices. Sections were dewaxed and stained with Perls Prussian blue stain to detect the presence of iron at light microscopy. In addition, a standard hematoxylin-eosin stain was performed. For coregistration of histological sections and MRI scans, the zone of ablation was used as a landmark.

Immunohistochemical staining of macrophages was performed using a primary antibody (rat anti–mouse CD11b clone M1/70.15, cross-reactivity to rabbit; Bio-Rad, 1:100), and Dako REAL Antibody Diluent (Dako, Denmark) required incubation overnight at 8 degrees. Sections were washed 2 times with phosphate buffered saline, pH 7.4. Macrophage binding was located by incubation with the polyclonal secondary antibody (goat anti–rat IgG HRP; Thermo Fisher Scientific, Germany, 1:200) and subsequently incubation with the Vector SG Substrate HRP Kit (Vector Laboratories, USA). Quantification of macrophages on CD11b staining and Perls Prussian blue–positive staining areas was assessed in serial sections (Figs. 2C, D).

To analyze the colocalization of areas positive for Perls Prussian blue staining and areas positive for CD11b, serial sections were stained. On digitized images, the Perls Prussian blue staining area was segmented and quantified using computer-assisted image analysis (ImageJ software, Version 1.51). By dividing the segmented area by the overall periablational area, the %Perls Prussian blue staining per periablational area was determined. The same procedure was used to measure the % CD11b immunostaining per periablational area. To evaluate the colocalization of areas positive for Prussian blue staining and CD11b + macrophages, the correlation of %Perls Prussian blue staining area and %CD11b immunostaining area was analyzed (Fig. 2B).

Inductively Coupled Plasma–Mass Spectrometry for Iron Quantification

Inductively coupled plasma–mass spectrometry (ICP-MS) was conducted using periablational rim tissue samples at each time point (n = 3 per group) as previously described.[28,29] In brief, after the last imaging session, liver tissue samples were digested at 37°C in 70% nitric acid overnight, followed by dilution with deionized water to an acid concentration of 2.5% for ICP-MS analysis. For each sample set, a standard curve was documented for iron concentration.

Laser Ablation–Inductively Coupled Plasma–Mass Spectrometry for Spatial Localization of Iron

Laser ablation–ICP-MS (LA-ICP-MS) analysis was performed as described previously[30,31] for quantitative elemental imaging of Fe and Zn to determine the iron distribution within the periablational rim after the injection of the SPION agent. X-ray spectra were acquired in the iron distribution, and the iron distribution was mapped. In addition, the P value was detected qualitatively. Tissues were cut at −20°C into 10 μm cryosections and immediately mounted on SuperFrost Plus Adhesion Slides (Thermo Scientific). The LA-ICP-MS analysis was performed with an LSX-213 G2+ laser system (Teledyne CETAC Technologies, Omaha, NE) equipped with a 2-volume HelEx II cell connected via Tygon tubing to an ICPMS-2030 (Shimadzu, Kyoto, Japan). Samples were ablated via line-by-line scan with a spot size of 15 μm, a scan speed of 45 μm/s, and 800 mL/min He as transport gas. The analysis was performed in collision gas mode with He as collision gas and 50 milliseconds integration time for the analyzed isotopes ^{31}P, ^{57}Fe, and ^{64}Zn. For the quantification of Fe and Zn, matrix-matched standards based on gelatin were used. Nine gelatin standards (10% wt/wt), including a blank, were spiked with different Fe and Zn concentrations ranging from 1 to 5000 μg/g for Fe and 1 to 500 μg/g for zinc. Averaged intensities of the scanned lines of the standards showed good linear correlation with a regression coefficient $R^2 > 0.996$ within this concentration range. Limit of detection and limit of quantification, calculated with the 3σ and 10σ criteria, were 3.0 μg/g and 10 μg/g for Fe and 0.8 μg/g and 2.5 μg/g for Zn, respectively. The quantification and visualization were performed with an in-house developed software (WWU Münster, Münster, Germany).

Statistical Analysis

The number of animals was determined by sample size calculation before the study (*t* test, type 1 error = 0.05, type 2 error = 0.2, effect size μΔ = 2.5). Statistical analysis was performed as previously described.[28–30] Values are expressed as mean ± standard deviation. The values of the different time points were compared with their controls using SigmaStat (Systat Software). A Student *t* test (unpaired, 2-tailed) was applied for the comparison of continuous variables. In case of more than 2 groups, statistical comparisons were performed by analysis of variance followed by the Bonferroni test. Univariate correlations were calculated using the Pearson correlation method. $P < 0.05$ was considered statistically significant.

RESULTS

The mean diameter of the VX2 tumors was 10.1 ± 0.17 mm. Radiofrequency ablation was technically successful in all 12 animals; the mean diameter of the ablation zone was 12.9 ± 2.4 mm. The difference in the diameter of the tumors and of the ablation zones in the 4 groups was not statistically significant ($P > 0.05$). After RFA, SPION-enhanced T2*-weighted MRI scans displayed a progressive increase in the area of the periablational rim demonstrating signal loss (dark pixel area) starting 1 week and peaking 3 weeks after ablation. Consistently, a gradual accumulation of iron-loaded macrophages in the periablational rim was observed at ex vivo histopathologic and immunochemistry staining. Sections stained for Perls Prussian blue and CD11b showed a progressive and significant accumulation of iron-loaded macrophages in the periablational rim: ex vivo %Perls Prussian blue and %CD11b staining area measurements over time demonstrated a tight correlation with the number of dark pixels in the periablational rim measured in vivo ($y = 2488.2x + 288.27$, $R^2 = 0.93$, $P < 0.05$ and $y = 83,661x − 735.63$, $R^2 = 0.90$, $P < 0.05$). Follow-up of MRI signal changes in the periablational rim showed a consecutive and significant decline in the rSI ratio after particle injection peaking at week 3 after RFA. In vivo macrophage MRI as well as the corresponding ex vivo histopathologic analysis of the periablational rim at consecutive time points are summarized in Figure 3.

Monitoring Macrophagic Accumulation in the Periablational Rim Using SPION-Enhanced MRI

On SPION-enhanced MRI scans acquired at baseline examination, the periablational rim appeared isointense to the liver parenchyma.
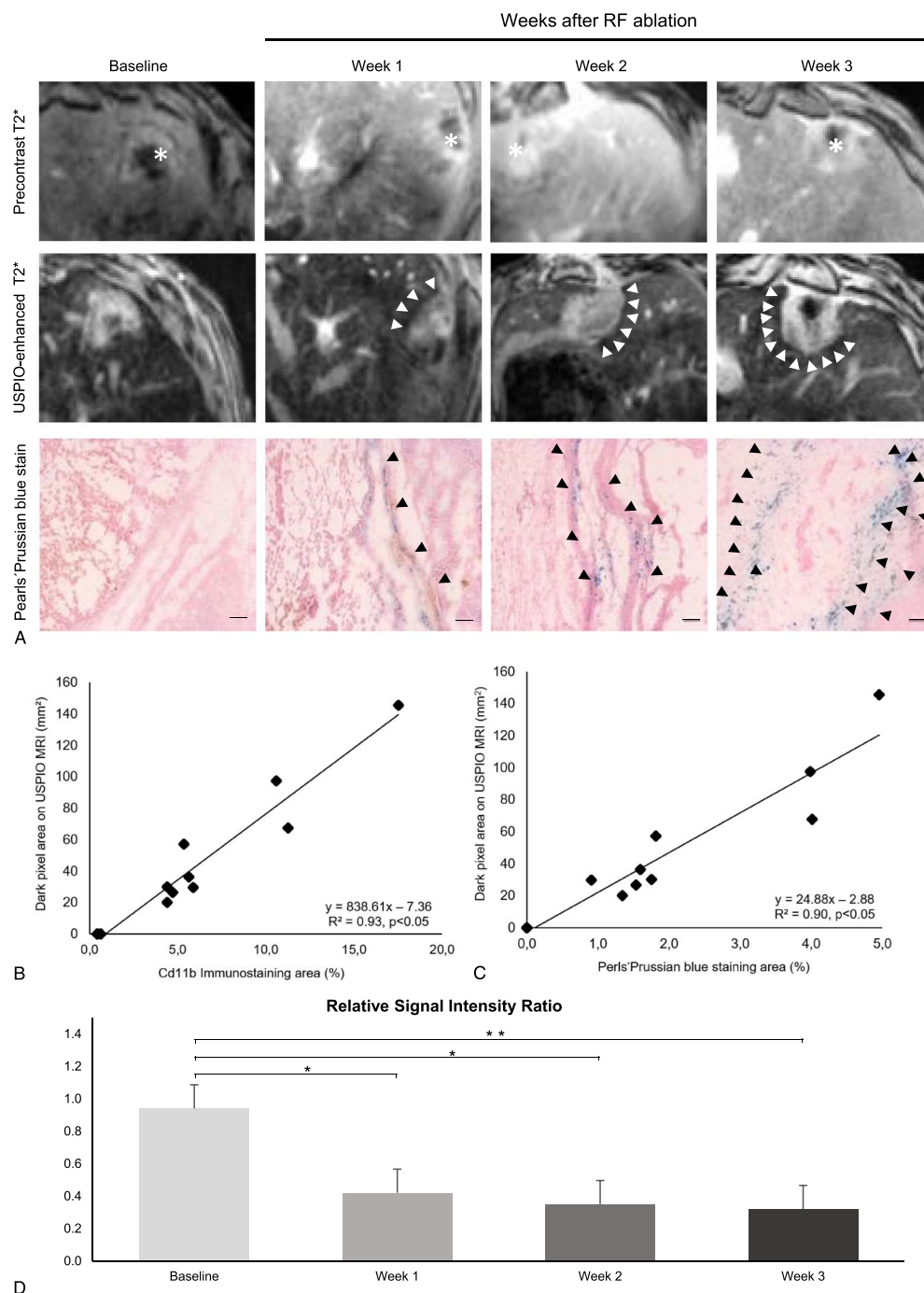
FIGURE 3. In vivo assessment of macrophagic accumulation in the periablational rim. A, In the horizontal direction, the images are ordered by the time of acquisition in relation to RFA. The first row shows precontrast T2*-weighted images acquired at day 1 of each time point from 4 different animals. Ablation zones are visible as inhomogeneous areas of hypointense liver parenchyma surrounded by a hyperintense peritumoral rim on T2*-weighted images (asterisk). The second row displays the T2*-weighted images acquired in the same animals 24 hours after intravenous administration of SPIONs, on day 2 of each time point. Although at baseline (week 0), no hypointense rim surrounding the ablation zone can be detected, SPION-enhanced T2*-weighted images acquired at weeks 1, 2, and 3 display a steadily growing band-like area of signal loss surrounding the ablation zone due to the progressive recruitment of iron-loaded macrophages in the periablational rim (white arrowheads). The third row shows photomicrographs of the periablational rim at each time point. Although at baseline virtually no blue-stained iron oxide particles are visible in the periablational rim, the images obtained at 1, 2, and 3 weeks visually demonstrate a steady and substantial increase of blue-stained particles corresponding to SPION-loaded macrophages (black arrowheads) infiltrating the liver parenchyma surrounding the zone of ablation. Scale bars indicate 100 μm. B and C, Scatter plots show a strong positive correlation between the in vivo measured number of dark pixels and ex vivo %CD11b and %Perls Prussian blue staining area measurements ($P < 0.05$ and $y = 836.61x - 7.36$, $R^2 = 0.93$, and $y = 24.88x - 2.88$, $R^2 = 0.90$, $P < 0.05$). D, Average relative signal intensity ratio (rSI ratio) at baseline and during follow-up. Compared with baseline examination, SPION-enhanced T2*-weighted images demonstrated a significant decline in the rSI ratio at week 1 ($P < 0.05$), week 2 ($P < 0.05$), and week 3 ($P < 0.01$).

Quantitative analysis of SI changes showed no significant decline in the SI of the periablational rim: the mean rSI ratio was 0.94 ± 0.2, indicating a signal decrease of 6%. One week after RFA (week 1), a thin hypointense rim surrounding the zone of ablation could be seen on SPION-enhanced T2*-weighted images. The area of the rim demonstrating signal loss measured 25.3 ± 0.3 mm^2 ($P < 0.001$). The mean rSI ratio decreased significantly from 0.94 ± 0.2 to 0.42 ± 0.1, indicating a signal decrease of 58% after SPION administration ($P = 0.02$). On week 2, the dark pixel area in the periablational rim further increased from 25.3 ± 0.3 mm^2 to 41.2 ± 0.1 mm^2 ($P = 0.1$). The mean rSI ratio decreased to 0.35 ± 0.1, indicating a significant signal decrease of 65% after SPION administration ($P = 0.01$). At the latest imaging time point after RFA (week 3), a circumferential rim of hypointense liver parenchyma could be seen around the zone of ablation.

The dark pixel area increased from 41.2 ± 0.1 mm^2 to 103.45 ± 0.6 mm^2 ($P = 0.06$). Between week 1 and week 3, the dark pixel area surrounding the zone of ablation increased from 25.3 ± 0.3 mm^2 to 103.45 ± 0.6 mm^2 ($P = 0.02$). The mean rSI ratio at 3 weeks was 0.31 ± 0.2, indicating an SPION-induced signal decrease of 69% ($P = 0.006$).

Histopathologic Evaluation of Macrophage Accumulation in the Periablational Rim

Hematoxylin-eosin staining allowed an anatomical overview of the histological sections and a reliable differentiation between healthy liver tissue and the ablation zone at each time point. No residual tumor cells could be detected in or adjacent to the ablation zone.

At baseline examination, immediately after RFA (week 0), no significant amount of iron-loaded macrophages was observed in the periablational rim. One week after RFA (week 1), sections stained for Perls Prussian blue showed multiple blue-stained cells corresponding to iron-loaded macrophages lining up at the margins of the ablation zone. The mean ex vivo %Perls Prussian blue staining area was 1.26% of the section. Serial histological sections stained for CD11b showed similar results with a mean %CD11b immunostaining area of 5.01%. Fourteen days after ablation (week 2), the mean ex vivo %Perls Prussian blue staining area increased slightly from 1.26% to 1.72% ($P = 0.08$) as well as the mean %CD11b immunostaining area increased from 5.01% to 5.63% ($P = 0.85$) of the section. At the latest monitoring time point, 3 weeks after RFA, Perls Prussian blue staining showed a thick rim of blue-stained, iron-loaded macrophages surrounding the ablation zone. Ex vivo %Perls Prussian blue staining area increased significantly from 1.72% to 4.3% ($P = 0.001$). %CD11b immunostaining area increased from 5.63% to 13.12% ($P = 0.02$).

Iron Concentration in the Periablational Rim by Inductively Coupled Plasma–Mass Spectrometry

The average concentration of iron in the periablational rim increased substantially in line with the accumulation of iron-loaded macrophages in the rim throughout the different time points. The ex vivo measured iron concentrations (ICP-MS) demonstrated a significant correlation with the in vivo dark pixels on SPION MRI ($y = 1.54x + 4.25$, $R^2 = 0.89$, $P < 0.05$) (Fig. 4A).

Spatial Localization of Iron by Laser Ablation–Inductively Coupled Plasma–Mass Spectrometry

Laser ablation–ICP-MS confirmed colocalization of targeted iron in the SPION probe with iron-loaded macrophages (Fig. 4B). The spatial distributions of phosphorus in the samples were mapped as control; however, no specific distribution pattern was observed.

DISCUSSION

This study demonstrates a significant correlation between the area of the periablational rim with signal loss on SPION-enhanced gradient echo MRI scans and the number of iron-containing macrophages in the periablational rim of RFA-treated VX2 tumor-bearing rabbits, thus establishing SPION-enhanced MRI as a valuable tool for the noninvasive quantification of RFA-induced perifocal macrophage recruitment.

Sterile liver injury as occurring in the context of thermal ablation is sensed by KCs that respond by releasing various cytokines that attract inflammatory monocytes from the circulation to the thermal injury site.[10,32] The MoMFs recruited to the site of liver injury initially display
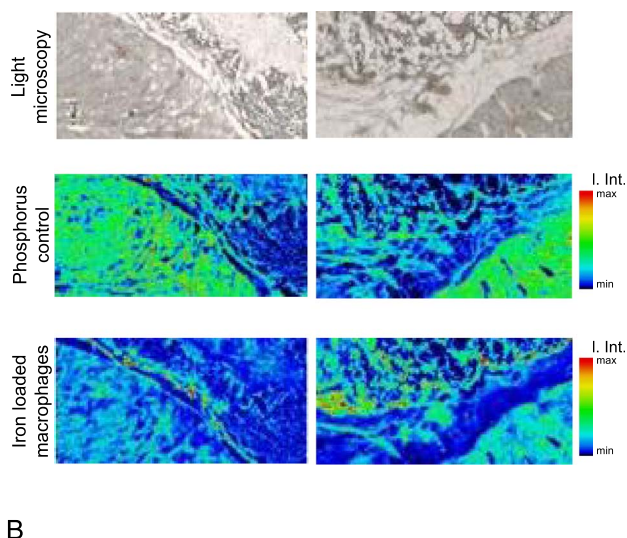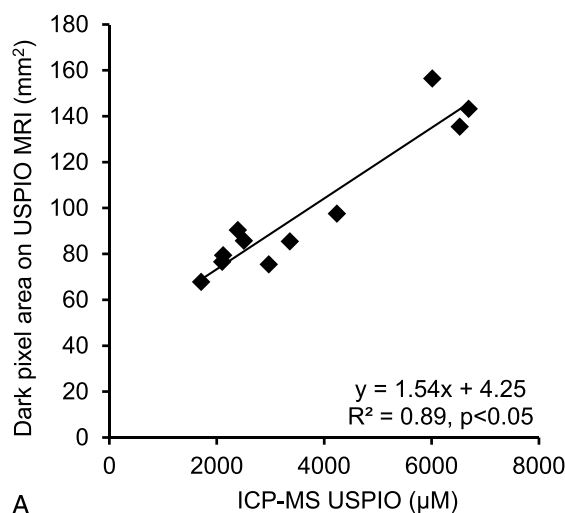
FIGURE 4. Correlation of in vivo MRI with inductively coupled plasma–mass spectrometry (ICP-MS) and spatial localization of iron oxide particles using laser ablation–inductively coupled plasma–mass spectrometry (LA-ICP-MS). A, A strong correlation of ICP-MS measurements for iron with in vivo measurements after the administration of SPIONs was demonstrated. B, Light microscopy images (B1 and B4) and phosphorus distribution (B2 and B5) were used to get an anatomical overview of the histological sections. LA-ICP-MS visualized the iron oxide particles within the periablational rim (B3 and B6, white arrowheads).

a proinflammatory phenotype and contribute to the exacerbation of inflammation by releasing macrophage-derived soluble mediators that perpetuate cellular injury, inhibit cell death, and promote hepatocyte proliferation.[33] After the acute phase of injury, both KCs and MoMFs cooperate in tissue repair and regeneration mechanisms trough the release of anti-inflammatory cytokines, growth factors, and angiogenic factors.[34–36] Proinflammatory cytokines (eg, IL-6) as well as proregenerative and proangiogenic factors (eg, HGF/c-Met and VEGF) have been shown to be key components of a mechanistic pathway that drives RFA-induced local and systemic tumor growth.[3,4,37,38] Clinical and preclinical studies have reported a dramatic hepatic and serologic upregulation of these key pro-oncogenic mediators after thermal ablation, and their selective inhibition by pharmacologic modulation has been shown to reduce RFA-induced pro-oncogenic effects.[13] Similarly, adjuvant liposomal clodronate has been proven to effectively suppress distant tumorigenic effects of hepatic RFA by reducing macrophages recruitment in the periablational rim, sanctioning the pivotal role of perifocal macrophage accumulation as a therapeutic target for upstream blocking of unwanted pro-oncogenic effects of thermal ablation.[39] Hence, noninvasive methods to image perifocal RFA-induced macrophagic accumulation in vivo would be extremely valuable to quantify and ultimately modulate ablation-induced pro-oncogenic effects thus improving clinical outcomes. Macrophage labeling with SPION has been previously established in various inflammatory and neoplastic diseases. Lefevre et al[40] demonstrated that, unlike gadolinium-enhanced MRI, SPION-enhanced MRI scans can accurately help monitor bacterial joint infection during antibiotic treatment by identifying areas of macrophage infiltration into infected synovium of rabbits. In a recent clinical study, Iv and colleagues[19] demonstrated a correlation between MRI measurements of susceptibility obtained after SPION administration and the concentration of iron-containing macrophages in high-grade gliomas, confirming the validity of SPION-enhanced MRI for in vivo macrophage imaging in patients with malignant tumors. By exploiting the cellular dysfunction caused in perifocal KCs by thermal ablation, SPION-enhanced MRI has also been successfully used for early visualization of the ablation margins in the context of hepatic RFA.[21–23] However, to the best of our knowledge, no studies assessed the use of SPION-enhanced MRI to quantify the RFA-induced inflammatory response. Our results indicate that SPION-enhanced MRI enables noninvasive quantification of macrophages in the periablational rim after RFA of VX2 tumor-bearing rabbits showing a gradual increase of cellular accumulation surrounding the ablation zone peaking at 3 weeks after ablation. The quantifiable number of dark pixels observed after SPION administration correlated with the histologically evaluated Perls Prussian blue staining area, providing radiological-pathological validation for our imaging findings. These results are in accordance with previous studies intended to characterize the cellular composition of the inflammatory periablational red zone and describing a progressive accumulation of macrophages at the border zone, with their number and ratio beginning to excel at 1 week after RFA.[4] To further validate our MRI findings, iron concentrations in the periablational rim were quantified using ICP-MS and LA-ICP-MS at each time point. Iron concentrations in the periablational rim closely reflected the area of signal loss after SPION application ($y = 1.54x + 4.25$, $R^2 = 0.89$, $P < 0.05$), displaying the highest iron concentrations at 3 weeks after RFA. Colocalization of the SPION probe with iron-loaded macrophages was confirmed by LA-ICP-MS. Our findings may pave the way for the use of SPION-enhanced MRI to study the extent of ablation-induced macrophage accumulation in conjunction with different sources of ablative energy and other locoregional therapies including embolotherapies. In fact, inflammatory activity in the periablational rim after local ablation has been shown to vary not only based on poorly understood patients' clinical conditions but also based on the ablative energy source and the heating strategy selected for treatment. Recently, Bulvik et al[41] compared both periablational and systemic effects of thermal RFA and nonthermal ablation with irreversible electroporation and reported a significantly

greater accumulation of macrophages surrounding the irreversible electroporation zone of ablation compared with RFA. On the other hand, Velez et al[42] recently showed that treatments with higher-temperature, short-duration microwave ablation resulted in reduced inflammatory cellular accumulation in the periablational rim, reduced expression of pro-oncogenic mediators (IL-6, VEGF, and HGF), and ultimately in reduced distant tumor growth compared with slower, lower-power microwave ablation or RFA protocols.

The VX2 cell line was chosen due to its biologically reproducible and predictable growth into discrete lesions after intrahepatic implantation. Moreover, the VX2 rabbit tumor model overcomes the intrinsic limitations of rodent models in terms of animal size allowing for both RFA and MRI experiments using clinically applied ablation instruments as well as clinical MRI scanners and imaging sequences. Several limitations to our study need to be acknowledged. First, the results were obtained in a small group of animals for feasibility and ethical reasons. Second, we used a single source of energy (RFA) and a standard setting to ensure comparable ablation zones throughout the different time points. Hence although perifocal inflammatory cell accumulation has been shown to occur also with other thermal and nonthermal techniques of ablation, the RFA of VX2 tumor-bearing rabbits was chosen for initial testing of preclinical proof of principle in vivo and is not generalizable for other forms of local ablation. Third, despite the fact that SPION are taken up by monocytes, KCs, and MoMFs, we did not distinguish between these populations on histological examinations. However, because these cellular components play an equally important role in the hepatic injury and repair process, we believe that this limitation does not unduly affect the validity of our results.[7,43] Fourth, due to the different staining techniques, a colocalization of both markers on 1 single slide was not possible. Both CD11 immunostaining and Perls Prussian blue staining were performed on serial sections. To evaluate the colocalization of areas positive for Perls Prussian blue staining and CD11b+ macrophages, we assessed the correlation of %Perls Prussian blue staining area and %CD11b immunostaining as shown in Figure 2B.

Lastly, although demonstrating a gradual increase in perifocal macrophage accumulation over time, our follow-up was not long enough to demonstrate the downward phase of macrophage accumulation into the rim. Hence, further studies may include longer follow-up windows or a control group in which macrophage recruitment in the rim is pharmacologically counteracted to clarify whether a reduction in macrophage accumulation can be measured equally well in vivo using SPION-enhanced MRI.

CONCLUSIONS

In conclusion, SPION-enhanced MRI enabled noninvasive quantification of the macrophage accumulation in the periablational rim of VX2 tumor-bearing rabbits after focal RFA. Given the pivotal role of macrophages in the genesis of ablation-induced tumorigenic effects and in light of studies sanctioning that upstream blocking of unwanted pro-oncogenic effects of thermal ablation is achievable by reducing perifocal cellular accumulation, a tool to noninvasively image perifocal RFA-induced macrophage accumulation in vivo might be valuable to quantify and ultimately modulate ablation-induced pro-oncogenic effects.

REFERENCES

1. European Association for the Study of the Liver. EASL clinical practice guidelines: management of hepatocellular carcinoma. *J Hepatol*. 2018;69:182–236.
2. Van Cutsem E, Cervantes A, Adam R, et al. ESMO consensus guidelines for the management of patients with metastatic colorectal cancer. *Ann Oncol*. 2016;27:1386–1422.
3. Rozenblum N, Zeira E, Scaiewicz V, et al. Oncogenesis: an "off-target" effect of radiofrequency ablation. *Radiology*. 2015;276:426–432.

4. Rozenblum N, Zeira E, Bulvik B, et al. Radiofrequency ablation: inflammatory changes in the periablative zone can induce global organ effects, including liver regeneration. *Radiology*. 2015;276:416–425.

5. Ahmed M, Kumar G, Moussa M, et al. Hepatic radiofrequency ablation-induced stimulation of distant tumor growth is suppressed by c-Met inhibition. *Radiology*. 2016;279:103–117.

6. Shan Z, Ju C. Hepatic macrophages in liver injury. *Front Immunol*. 2020;11:322.

7. Tacke F. Targeting hepatic macrophages to treat liver diseases. *J Hepatol*. 2017; 66:1300–1312.

8. Tacke F, Zimmermann HW. Macrophage heterogeneity in liver injury and fibrosis. *J Hepatol*. 2014;60:1090–1096.

9. Guillot A, Tacke F. Liver macrophages: old dogmas and new insights. *Hepatol Commun*. 2019;3:730–743.

10. Dal-Secco D, Wang J, Zeng Z, et al. A dynamic spectrum of monocytes arising from the in situ reprogramming of CCR2+ monocytes at a site of sterile injury. *J Exp Med*. 2015;212:447–456.

11. Ahmed M, Kumar G, Navarro G, et al. Systemic siRNA nanoparticle-based drugs combined with radiofrequency ablation for cancer therapy. *Plos One*. 2015; 10:e0128910.

12. Ahmed M, Kumar G, Gourevitch S, et al. Radiofrequency ablation (RFA)–induced systemic tumor growth can be reduced by suppression of resultant heat shock proteins. *Int J Hyperthermia*. 2018;34:934–942.

13. Erinjeri JP, Thomas CT, Samoilia A, et al. Image-guided thermal ablation of tumors increases the plasma level of interleukin-6 and interleukin-10. *J Vasc Interv Radiol*. 2013;24:1105–1112.

14. Hauger O, Grenier N, Deminere C, et al. USPIO-enhanced MR imaging of macrophage infiltration in native and transplanted kidneys: initial results in humans. *Eur Radiol*. 2007;17:2898–2907.

15. Bierry G, Jehl F, Boehm N, et al. Macrophage imaging by USPIO-enhanced MR for the differentiation of infectious osteomyelitis and aseptic vertebral inflammation. *Eur Radiol*. 2009;19:1604–1611.

16. Lancelot E, Raynaud JS, Desché P. Current and future MR contrast agents: seeking a better chemical stability and relaxivity for optimal safety and efficacy. *Invest Radiol*. 2020;55:578–588.

17. Wang YX, Hussain SM, Krestin GP. Superparamagnetic iron oxide contrast agents: physicochemical characteristics and applications in MR imaging. *Eur Radiol*. 2001;11:2319–2331.

18. Smits LP, Coolen BF, Panno MD, et al. Noninvasive differentiation between hepatic steatosis and steatohepatitis with MR imaging enhanced with USPIOs in patients with nonalcoholic fatty liver disease: a proof-of-concept study. *Radiology*. 2016;278:782–791.

19. Iv M, Samghabadi P, Holdsworth S, et al. Quantification of macrophages in high-grade gliomas by using ferumoxytol-enhanced MRI: a pilot study. *Radiology*. 2019;290:198–206.

20. Smits LP, Tiessens F, Zheng KH, et al. Evaluation of ultrasmall superparamagnetic iron-oxide (USPIO) enhanced MRI with ferumoxytol to quantify arterial wall inflammation. *Atherosclerosis*. 2017;263:211–218.

21. Mori K, Fukuda K, Asaoka H, et al. Radiofrequency ablation of the liver: determination of ablative margin at MR imaging with impaired clearance of ferucarbotran—feasibility study. *Radiology*. 2009;251:557–565.

22. Nagai M, Yamaguchi M, Mori K, et al. Magnetic resonance-based visualization of thermal ablative margins around hepatic tumors by means of systemic ferucarbotran administration before radiofrequency ablation: animal study to reveal the connection between excess iron deposition and T2*-weighted hypointensity in ablative margins. *Invest Radiol*. 2015;50:376–383.

23. Koda M, Tokunaga S, Miyoshi K, et al. Ablative margin states by magnetic resonance imaging with ferucarbotran in radiofrequency ablation for hepatocellular carcinoma can predict local tumor progression. *J Gastroenterol*. 2013;48:1283–1292.

24. Goldberg SN, Gazelle GS, Compton CC, et al. Radio-frequency tissue ablation of VX2 tumor nodules in the rabbit lung. *Acad Radiol*. 1996;3:929–935.

25. Bierry G, Jehl F, Boehm N, et al. Macrophage activity in infected areas of an experimental vertebral osteomyelitis model: USPIO-enhanced MR imaging—feasibility study. *Radiology*. 2008;248:114–123.

26. Bierry G, Lefevre S, Dietemann JL, et al. In vivo macrophage imaging using MR targeted contrast agent for longitudinal evaluation of septic arthritis. *J Vis Exp*. 2013;:e50296.

27. Kooi ME, Cappendijk VC, Cleutjens KB, et al. Accumulation of ultrasmall superparamagnetic particles of iron oxide in human atherosclerotic plaques can be detected by in vivo magnetic resonance imaging. *Circulation*. 2003;107: 2453–2458.

28. Reimann C, Brangsch J, Kaufmann JO, et al. Dual-probe molecular MRI for the in vivo characterization of atherosclerosis in a mouse model: simultaneous assessment of plaque inflammation and extracellular-matrix remodeling. *Sci Rep*. 2019;9:13827.

29. Botnar RM, Brangsch J, Reimann C, et al. In vivo molecular characterization of abdominal aortic aneurysms using fibrin-specific magnetic resonance imaging. *J Am Heart Assoc*. 2018;7:e007909.

30. Brangsch J, Reimann C, Kaufmann JO, et al. Concurrent molecular magnetic resonance imaging of inflammatory activity and extracellular matrix degradation for the prediction of aneurysm rupture. *Circ Cardiovasc Imaging*. 2019;12:e008707.

31. Adams LC, Brangsch J, Reimann C, et al. Simultaneous molecular MRI of extracellular matrix collagen and inflammatory activity to predict abdominal aortic aneurysm rupture. *Sci Rep*. 2020;10:15206.

32. Karlmark KR, Weiskirchen R, Zimmermann HW, et al. Hepatic recruitment of the inflammatory Gr1+ monocyte subset upon liver injury promotes hepatic fibrosis. *Hepatology*. 2009;50:261–274.

33. Jaeschke H, Williams CD, Ramachandran A, et al. Acetaminophen hepatotoxicity and repair: the role of sterile inflammation and innate immunity. *Liver Int*. 2012; 32:8–20.

34. Fadok VA, Bratton DL, Konowal A, et al. Macrophages that have ingested apoptotic cells in vitro inhibit proinflammatory cytokine production through autocrine/paracrine mechanisms involving TGF-beta, PGE2, and PAF. *J Clin Invest*. 1998; 101:890–898.

35. McDonald PP, Fadok VA, Bratton D, et al. Transcriptional and translational regulation of inflammatory mediator production by endogenous TGF-beta in macrophages that have ingested apoptotic cells. *J Immunol*. 1999;163:6164–6172.

36. Huynh ML, Fadok VA, Henson PM. Phosphatidylserine-dependent ingestion of apoptotic cells promotes TGF-beta1 secretion and the resolution of inflammation. *J Clin Invest*. 2002;109:41–50.

37. Chapiro J, Geschwind JF. Science to practice: the changing face of local tumor therapies-do we have to think systemically when treating cancer locally? *Radiology*. 2015;276:315–317.

38. Shi LR, Wang JJ, Ding NH, et al. Inflammation induced by incomplete radiofrequency ablation accelerates tumor progression and hinders PD-1 immunotherapy. *Nat Commun*. 2019;10:5421.

39. Kumar G, Goldberg S, Wang Y, et al. 3:48 PM, Abstract No. 148. Adjuvant liposomal clodronate reduces periablational inflammatory cell recruitment and "off-target" stimulation of distant tumor growth after hepatic radiofrequency ablation (RFA). *J Vasc Intervent Radiol*. 2015;26:S71.

40. Lefevre S, Ruimy D, Jehl F, et al. Septic arthritis: monitoring with USPIO-enhanced macrophage MR imaging. *Radiology*. 2011;258:722–728.

41. Bulvik BE, Rozenblum N, Gourevich S, et al. Irreversible electroporation versus radiofrequency ablation: a comparison of local and systemic effects in a small-animal model. *Radiology*. 2016;280:413–424.

42. Velez E, Goldberg SN, Kumar G, et al. Hepatic thermal ablation: effect of device and heating parameters on local tissue reactions and distant tumor growth. *Radiology*. 2016;281:782–792.

43. Chouly C, Pouliquen D, Lucet I, et al. Development of superparamagnetic nanoparticles for MRI: effect of particle size, charge and surface nature on biodistribution. *J Microencapsul*. 1996;13:245–255.